X-Ray Compton Profiles of Li and Na: Theory and Experiments

P. Eisenberger, L. Lam,* P. M. Platzman, and P. Schmidt
Bell Telephone Laboratories, Murray Hill, New Jersey 07974
(Received 26 May 1972)

A general discussion is presented of x-ray Compton profiles for conduction electrons in metals. A formalism that includes both the interelectron Coulomb interaction and the electron-ion interaction is then introduced. X-ray-scattering measurements of the Compton profiles of single-crystal Li and polycrystalline Na were carried out at room temperature. There is substantial agreement between our experimental data and the theoretical predictions.

I. INTRODUCTION

Following the discovery and explanation of the Compton effect, it was suggested by several people that this effect might be useful for measuring the electronic momentum density of a variety of systems.[1,2] Recently, there has been renewed interest in utilizing this rather unique microscopic probe.[3-6]

In a typical experiment,[6] incident x rays with frequency ω_1, wave vector $\vec{k}_1$, and polarization $\vec{\epsilon}_1$ are scattered into a small solid angle. The scattered x ray is described by the corresponding quantities ω_2, $\vec{k}_2$, and $\vec{\epsilon}_2$ (see Fig. 1). The cross section may be completely characterized by the two quantities:

$$\omega \equiv \omega_1 - \omega_2, \quad \vec{k} \equiv \vec{k}_1 - \vec{k}_2 , \tag{1}$$

which are, respectively, the energy and momentum transferred to the medium. In the so-called impulse approximation,[2] the cross section is given by

$$\frac{d\sigma}{d\omega\, d\Omega} = \left(\frac{d\sigma}{d\Omega}\right)_0 \left(\frac{\omega_1}{\omega_2}\right) \int d^3p\, N_{\vec{p}}\, \delta\left(\omega - \frac{k^2}{2m} - \frac{\vec{k}\cdot\vec{p}}{m}\right)$$

$$\equiv \left(\frac{d\sigma}{d\Omega}\right)_0 \left(\frac{\omega_1}{\omega_2}\right) \frac{m}{k}\, J(q) , \tag{2}$$

where

$$\left(\frac{d\sigma}{d\Omega}\right)_0 \equiv \left(\frac{e^2}{mc^2}\right)^2 (\vec{\epsilon}_1 \cdot \vec{\epsilon}_2)^2 \left(\frac{\omega_2}{\omega_1}\right)^2 \tag{3}$$

is the Thompson cross section. The momentum density $N_{\vec{p}}$ is defined by,

$$N_{\vec{p}} \equiv \langle a^\dagger_{\vec{p}}\, a_{\vec{p}} \rangle , \tag{4}$$

where $\langle\ \rangle$ denotes the exact ground-state average of the free-fermion annihilation ($a_{\vec{p}}$) and creation ($a^\dagger_{\vec{p}}$) operators. Choosing the z axis as the direction of $\vec{k}$, the Compton profile is

$$J(q) \equiv \int dp_x\, dp_y\, [N_{\vec{p}}]_{p_z = q} , \tag{5}$$

with

$$q = (\tfrac{1}{2} k - m\omega/k) . \tag{6}$$

Equation (2) is valid as long as the energy of the x ray is small compared to mc^2 but large enough so that the recoil energy $\hbar^2 k^2/2m$ is much greater than the characteristic energies of the system being studied.

The momentum density $N_{\vec{p}}$ can be simply related to the Fourier transform of the many-electron wave function. The Compton profiles then serve as a useful check of the different approximate theoretical calculations of these wave functions. Most of the published work, attempting to interpret Compton profiles, has concentrated on two quite different types of physical systems: (a) Several groups have attempted to fit the Compton spectra of simple atoms and molecules,[5-7] and (b) a discussion of the Compton profiles of the conduction electrons in some simple metals has been given.[8]

In this paper, we will concentrate on the problem of the momentum density of the conduction electrons in simple metals. From a theoretical point of view, the momentum density of these simple metals is an interesting one. Wave functions of the conduction electrons in metals are, as a rule, calculated in the one-electron self-consistent-field approximation.[9] While the accuracy of such wave functions to describe the momentum density remains to be tested, the more fundamental question is whether we have to go beyond the one-electron formulation to realistically interpret the experimental Compton profiles for metals. This is the spirit which underlies our present investigations.

The deviations from free-electron behavior arises from a number of different sources. The Coulomb interactions between electrons and the interaction of the electrons with the ion cores give rise to the final correlated momentum density.

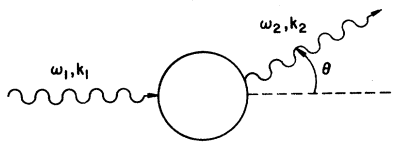

FIG. 1. Schematic description of the incoherent photon scattering.

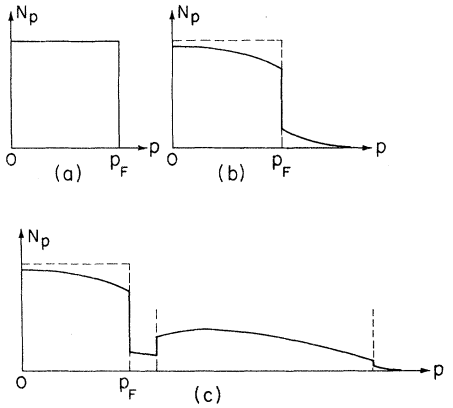

FIG. 2. Momentum density of electron gas: (a) noninteracting, (b) homogeneous interacting, (c) inhomogeneous interacting.

The interplay of these two effects are best illustrated in lithium and sodium. They both have bcc structure and almost the same electron densities but differ in the strength of electron-ion interaction by an order of magnitude. In fact, sodium, as we shall see, is very close to a homogeneous electron gas, i.e., the interactions of the conduction electrons with the ion cores are small. In this alkali the interelectron Coulomb interactions are dominant. Lithium, on the other hand, has a larger electron density but a nontrivial amount of electron-ion interactions, and both effects are significant. Since neither the homogeneous interacting electron gas nor the inhomogeneous noninteracting gas are exactly soluble, our approach to the problem must be approximate.

The earliest theoretical work on the subject of the momentum density in an interacting electron liquid focused on the behavior of the completely homogeneous system.[10-14] The Coulomb interaction was handled by treating it as weak. Recently, some preliminary discussion of the momentum density in the inhomogeneous system has been given by Lundqvist and Lydén.[8] Their treatment, like ours, is approximate. Unfortunately, the exact nature of these approximations and their limits of validity have not been accurately defined. In this paper, we will present a first-principles, but approximate, treatment of the interacting inhomogeneous electron fluid. Our approach will be to treat the inhomogenities to lowest order and relate the exact second-order momentum density to the exact response function of the homogeneous system. Assuming that the homogeneous system is accurately characterized by random-phase-approximation (RPA) theory, we will compare our theoretical results with experimental spectra taken in single crystals of Li and polycrystalline Na.

II. QUALITATIVE CONSIDERATIONS

At zero temperature the three-dimensional momentum density of a noninteracting homogeneous electron gas is the Fermi distribution [Fig. 2(a)]. This square three-dimensional distribution when integrated over the two directions perpendicular to the momentum transfer $\vec{k}$ [see Eq. (5)] gives the characteristic parabolic Compton profile [Fig. 3(a)]. When the interelectron Coulomb interactions are turned on, we expect a tail to appear in the momentum density beyond the Fermi momentum p_F. The discontinuity at p_F persists but its value is reduced from one to Z_{p_F}, the renormalization constant [Fig. 2(b)]. This altered three-dimensional distribution yields (integrating over the two directions perpendicular to $\hat{k}$) a curve with a smaller break in slope at p_F and a long tail [Fig. 3(b)]. The area under each curve in Fig. 3 is the same, i.e., proportional to the number of electrons. The finiteness of the average kinetic energy $\langle K.E. \rangle$

$$\langle K.E. \rangle = \int N_{\vec{p}}(p^2/2m)\, d^3p \tag{7}$$

implies that the tail in $N_{\vec{p}}$ falls off at least as fast as $|p|^{-6}$.

Accurate first-principles calculations of the momentum density can only be performed for weakly interacting fermion systems. The results of an RPA calculation of the momentum density for an electron gas[10] at the density of metallic sodium ($r_s = 3.97$) are displayed in Fig. 4. The quantity r_s is defined by $(3/4\pi n)^{1/3}$ in atomic units, where n is the electron density. Qualitatively, it is as expected. The tail in the momentum density falls off as p^{-8} and $Z_{p_F} = 0.51$.

When such a system of interacting electrons is submerged in a lattice of static ions, as in the case of metals, the momentum density $N_{\vec{p}}$ changes in two significant ways.[15] First, the sphere in momentum space centered at $p = 0$ becomes, in gen-

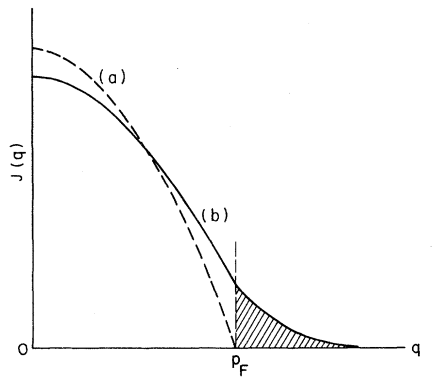

FIG. 3. Compton profiles of electron gas: curve (a), noninteracting; curve (b), homogeneous interacting.

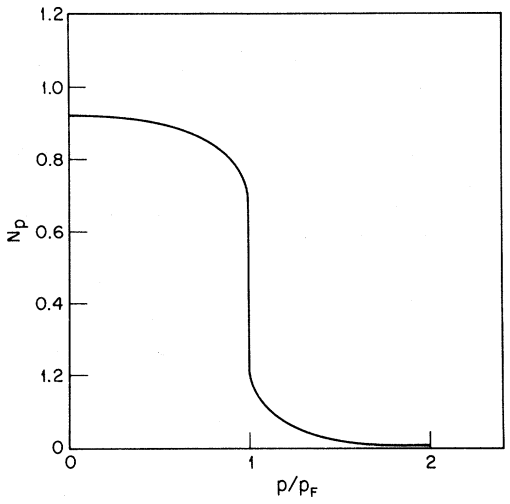

FIG. 4. Calculated momentum density of homogeneous electron gas (Ref. 10), $r_s = 3.97$.

eral, an anisotropic surface enclosing the same volume as before (Luttinger's theorem).[16] We call this the main m surface. Second, new surfaces identical to the one at $p = 0$ appear centered on each of the other reciprocal-lattice points. These are called secondary m surfaces. All these m surfaces are the images of the Fermi surface of the metal across which $N_{\vec{p}}$ suffers some discontinuity. They may be completely separate from each other or overlap in part, depending on the geometry of the lattice and the electron-ion interaction. The discontinuity of $N_{\vec{p}}$ at the main m surface is, in general, reduced from Z_{p_F}, the case without the ions. Similarly, the discontinuity at the secondary m surfaces is, in general, smaller than that at the main m surface. In contrast to the one-electron approximation (the band picture), there is no region in the momentum space where $N_{\vec{p}}$ is identically zero. Of course, the integral of $N_{\vec{p}}$ over the whole momentum space is still conserved. This means that $N_{\vec{p}}$ is reduced inside the main m surface, the intensity being transferred to the secondary m surfaces. The general qualitative picture for a weakly inhomogeneous system is that $N_{\vec{p}}$ is large within the m surfaces especially the main one, and relatively weak outside these surfaces. An example of this behavior is sketched in Fig. 2(c).

Equations (2) and (5) imply that for a fixed direction of the momentum transfer $\hat{k}$, the Compton profile actually measures the amount of $N_{\vec{p}}$ contained in a plane perpendicular to $\hat{k}$ sweeping through the momentum space. The profile will have a cusplike behavior whenever the plane touches one of the m surfaces. In addition to the sharp one where the plane last touches the main m surfaces as one moves away from the origin towards large k, there will be secondary cusp points when the plane happens to be tangent to other parts of the main m surface (secondary cusp points of the first kind). This does not happen for a spherical Fermi surface. A second kind of secondary cusp behavior exhibits itself even if the Fermi surface is spherical. These breaks appear when the integration plane touches the secondary m surfaces. These results follow from our general discussion of the $N_{\vec{p}}$ function and the fact that the sharpness of the break in the Compton profile reflects the amount of discontinuity present in $N_{\vec{p}}$ across the m surfaces.

For a metal, secondary cusp points always exist, although they may be difficult to detect. The secondary cusp points of the first kind (main m surface) provide information on the shape of the Fermi surface. The distance between the two main cusp points measures the distance in momentum space between the two planes perpendicular to $\hat{k}$ which touch and sandwich the Fermi surface from outside.[15] The secondary cusp points of the second kind reflect the position of the reciprocal-lattice vectors and hence the size and structure of the crystal.

The anisotropy of the Compton profiles for different directions of $\hat{k}$ relative to the crystal axis is due to the geometrical arrangement of the secondary m surfaces and the nonsphericity of each m surface. For simple metals like the alkalis, the former definitely outweighs the latter.

In Sec. III, a general formalism which allows us to compute $N_{\vec{p}}$ taking both the Coulomb correlation and crystal effects into account will be presented.

III. GENERAL FORMALISM

A. Momentum Density of the Weakly Inhomogeneous Electron Gas

Our method of finding the momentum density of an inhomogeneous electron liquid described by the Hamiltonian H is based on the two facts[17]: (i)

$$N_p = \left(\frac{\partial E_p(\lambda)}{\partial \lambda} \right)_{\lambda=0} , \tag{8}$$

where $E_p(\lambda)$ is the exact ground-state energy of $H_p(\lambda)$, and

$$H_p(\lambda) \equiv H + \lambda\, a_p^\dagger a_p . \tag{9}$$

Here $p \equiv (\vec{p}, \sigma_p)$ denotes the momentum and spin of the plane-wave state of an electron. The Hamiltonian H contains both the Coulomb interactions among conduction electrons and the interactions of these electrons with the ion cores.

(ii) In the graphical perturbation calculations of $E_p(\lambda)$, the same graph rules and same set of graphs

devised for the homogeneous electron gas can be adopted. The only difference being that we replace $\epsilon_k \equiv k^2/2m \equiv \epsilon_{\vec{k},\sigma_k}$ by

$$\epsilon_k(p) \equiv \epsilon_k + \lambda\delta_{k,p} \quad . \tag{10}$$

Rule (i) follows directly from Feynman's theorem.[18] It relies on the fact that the normalization of the ground state of $H_p(\lambda)$ is independent of λ. Rule (ii) is not completely trivial since one might suppose that the distribution function appearing in the zero-order Green's functions which characterize the perturbation theory could also be modified by λ. The essential point is that this distribution does not change. The Hamiltonians

$$T \equiv \sum_k \epsilon_k a_k^\dagger a_k \tag{11}$$

and

$$T_p \equiv \sum_k \epsilon_k(p)\, a_k^\dagger a_k \tag{12}$$

have the same ground state. In T_p we have only changed the energy of a single state p. The only way the Fermi distribution could change is if $\lambda > |\epsilon_{\vec{p}} - \epsilon_{\vec{p}_F}|$, and since we are interested in the limit $\lambda \to 0$, rule (ii) follows.

For an interacting electron gas in an external potential, the Hamiltonian is defined by

$$H = T + H_C + H_x \, , \tag{13}$$

where T is given in Eq. (11). The Hamiltonian H_C characterizes the pairwise Coulomb interaction between electrons, and H_x—that part due to the external potential.

When the external field is weak, H_x in Eq. (13) can be treated as the perturbation while $T + H_C$ can, at least formally, be treated exactly. The same situation holds for $H_p(\lambda)$ defined by Eq. (9). To second order in H_x we have

$$E_p(\lambda) = \langle 0 | T_p + H_C | 0 \rangle + \langle 0 | H_x | 0 \rangle + \sum_{m \neq 0} \frac{\langle 0 | H_x^\dagger | m \rangle \langle m | H_x | 0 \rangle}{E^0 - E^m} \, , \tag{14}$$

where $|0\rangle (|m\rangle)$ is the exact ground (excited) state of $T_p + H_C$ with energy $E^0(E^m)$. Combining Eqs. (8) and (14) we find that

$$N_p = N_p^0 + \Delta N_p \, , \tag{15}$$

where N_p^0 is the momentum density of a homogeneous electron gas and

$$\Delta N_p = \left[\frac{\partial}{\partial \lambda} \left(\langle 0 | H_x | 0 \rangle + \sum_{m \neq 0} \frac{\langle 0 | H_x^\dagger | m \rangle \langle m | H_x | 0 \rangle}{E^0 - E^m} \right) \right]_{\lambda = 0} . \tag{16}$$

In this way, the pairwise Coulomb interaction is included to all orders while the external potential is taken to second order.

For electrons in metals,

$$H_x = \sum_{\vec{G}} V_{\vec{G}} \rho_{-\vec{G}} \, , \tag{17}$$

where

$$\rho_{-\vec{G}} = \sum_{\vec{p},\sigma} a^\dagger_{\vec{p}+\vec{G},\sigma} a_{\vec{p},\sigma} \tag{18}$$

and

$$V(x) = \sum_{\vec{G}} V_{\vec{G}}\, e^{i\vec{G}\cdot\vec{x}} \tag{19}$$

is the potential energy due to the interaction of the electrons with static ions. The $\vec{G}$'s are the nonzero reciprocal-lattice vectors of the metal. The first term in Eq. (16) vanishes because of the translational invariance of $T_p + H_C$. Equation (16) then becomes

$$\Delta N_p = \sum_{\vec{G}} |V_{\vec{G}}|^2 \left(\frac{\partial}{\partial \lambda} \sum_{m \neq 0} \frac{|\langle m | \rho_{-\vec{G}} | 0 \rangle|^2}{E^0 - E^m} \right)_{\lambda = 0} . \tag{20}$$

Recalling the definition of the dielectric function $\epsilon(\vec{q},\omega)$ of a homogeneous electron gas,

$$[\epsilon(\vec{q},\omega)]^{-1} = 1 + v_q \sum \frac{2\omega_{m0} |\langle m | \rho_{-\vec{q}} | 0 \rangle|^2}{(\omega + i\delta)^2 - \omega_{m0}^2} \, , \tag{21}$$

with

$$v_q \equiv 4\pi e^2/q^2 \, , \quad q \neq 0$$
$$\equiv 0 \, , \quad q = 0 \tag{22}$$

and

$$\omega_{m0} \equiv E^m - E^0 \, . \tag{23}$$

We see then that

$$\Delta N_p = \tfrac{1}{2} \sum_{\vec{G}} \frac{1}{v_G} \left| \frac{V_{\vec{G}}}{\epsilon(\vec{G},0)} \right|^2 \left(\frac{\partial \epsilon_p(\vec{G},0)}{\partial \lambda} \right)_{\lambda = 0} \, , \tag{24}$$

where $\epsilon_p(\vec{G},0)$ is the dielectric function corresponding to the Hamiltonian $H_p(\lambda)$. Equation (24) is the principle result of this section. It makes sense only if the denominator does not vanish. For bcc crystals like Li and Na, $|\vec{G}|$ is always greater than two times the Fermi momentum and Eq. (24) is well defined. With rule (ii) in mind, utilizing an explicit form for the dielectric function of a homogeneous electron gas, ΔN_p can be obtained in analytic form.

Before evaluating Eq. (24) in a particularly simple approximation, we would like to consider how $V_{\vec{G}}$ may be related to a more physical quantity which is directly measurable. This may be done by using our model Hamiltonian H defined in Eqs. (13) and (17) to calculate, for example, the band gaps present in the one-electron band structure. To the extent that the response of the electron gas to the external potential is linear, as we have already assumed in deriving Eq. (24), the band gap in the direction of $\vec{G}$ is given by[19]

$$\Delta_G = 2 \left| Z_{p_F} \tilde{\Lambda}_4^\infty V_{\vec{G}} / \epsilon(\vec{G},0) \right| \, , \tag{25}$$

where Z_{p_F} is the quasiparticle renormalization constant and $\tilde{\Lambda}_4^\infty$ is the proper vertex part.[20]

B. Simplifications in RPA

The most general form of the static dielectric function is formally given by

$$\epsilon(\vec{G},0)=1-v_G Q(\vec{G},0)\ , \tag{26}$$

where $Q(\vec{G},0)$ is the electron polarization function. In RPA, $Q(\vec{G},0)$ is taken to be the free-electron polarizability given by

$$Q^0(\vec{G},0)=\sum_{\vec{p},\sigma}(n^0_{\vec{p},\sigma}-n^0_{\vec{p}+\vec{G},\sigma})/(\epsilon_{\vec{p}+\vec{G},\sigma}-\epsilon_{\vec{p},\sigma})\ , \tag{27}$$

where $n^0_{\vec{p}}\equiv n^0_{\vec{p},\sigma}$ is the noninteracting Fermi distribution. In this approximation [combining Eqs. (24) and (26)],

$$\Delta N_{\vec{p}}\equiv\sum_\sigma \Delta N_{\vec{p},\sigma}$$

$$=\sum_{\vec{G}}|\ W_{\vec{G}}\ |^2 M_{\vec{p}}(\vec{G})\ , \tag{28}$$

with

$$M_{\vec{p}}(\vec{G})\equiv\sum_{\vec{p}'}(n^0_{\vec{p}'}-n^0_{\vec{p}'+\vec{G}})(\delta_{\vec{p}'+\vec{G},\vec{p}}-\delta_{\vec{p}',\vec{p}})/(\epsilon_{\vec{p}'+\vec{G}}-\epsilon_{\vec{p}'})^2 \tag{29}$$

and

$$W_{\vec{G}}\equiv\tfrac{1}{2}\Delta_{\vec{G}}/|\,Z_{p_F}\tilde{\Lambda}^\infty_4\,|\ . \tag{30}$$

In this approximation $\Delta N_{\vec{p}}$ is exactly the second-order correction to the momentum density (second order in the external potential) for a free-electron gas in the presence of an appropriately screened $V_{\vec{G}}$, i.e., $W_{\vec{G}}$. The discontinuities in this additional momentum density $\Delta N_{\vec{p}}$ reflect the discontinuity in the $n^0_{\vec{p}}$, i.e., in the spherically symmetric interacting homogeneous electron liquid. For this reason we would expect Eq. (29) to apply to systems which, to a large extent, have an almost spherical Fermi surface. Most of the alkalis including Li are materials of this kind.

IV. EXPERIMENT

The general experimental procedure is well documented in the literature[6,7] and will not be described here. The experiments were carried out at room temperature and a scattering angle of 170°. One significant difference in this study is the use of a LiF(600) analyzing crystal to obtain higher resolution. Because of the sharp discontinuity in $J(q)$ expected at the Fermi surface, the Fourier-transform method was not used to remove finite resolution effects. The trial-and-error approach described by Phillips and Weiss[3] was used instead. A main problem in studying the conduction electrons in Li and Na is the subtraction of the contribution of the core electrons. The same procedure described in previous work,[6] used in removing the 1s electron contributions in N_2, O_2, and Ne was used to remove the contribution from the core electrons. A check was made after the subtraction to see if the ratio of the area under the core profile to the area under the conduction electron profile was 2 to 1 in Li and 10 to 1 in Na. The ratios were correct within 1%. For Na impulse approximation corrections were made for the 1s electrons.

There have been numerous Compton scattering experiments performed on Li[3,4,21–23] and one on Na.[3] The previous Li experiments have failed to discern any anisotropy in the Compton profiles and have been performed on samples which are so thick that multiple-scattering effects were undoubtedly significant. The previous Na experiments did not give quantitative results and in addition failed to consider corrections to the impulse approximation in subtracting the 1s core contributions. In this work, the anisotropy of the momentum density in Li was detected. Multiple-scattering effects were evaluated, and corrections to the impulse approximation were made for the inner-shell electrons in Na.

A. Na Experiments

The Na samples were studied in a vacuum chamber. Both silver and molybdenum radiation were used to remove ambiguities about impulse corrections. Since Na has the sharpest profile of any measured Compton profile, the resolution corrections are very large. Further studies were made of the resolution corrections by making measurements on polycrystalline Na using Ag radiation and a LiF(400) analyzing crystal, Mo radiation and a LiF(400) analyzing crystal, and finally Ag radiation and a LiF(600) analyzing crystal. Thus, a range of approximately 50% in experimental resolution was spanned. The data were analyzed independently for each case and the finite resolution effects were removed. The final results were compared and the agreement was good enough (less than 2% differences at $q=0$) that one had considerable confidence that one was correctly evaluating the finite resolution effects. In other words, the previously described recipe[6] for determining the resolution function was capable of spanning the 50% range in experimental resolution. The final data are essentially the results obtained using Ag radiation with the LiF(600) analyzing crystal. The Mo experiments using the LiF(400) analyzing crystal were used in the core electron region ($q>2$) to help give an accurate subtraction of the core contribution. The results for polycrystalline Na are given in Table I and Fig. 5. For illustration, the experimental results for Na utilizing Ag radiation before resolution corrections using LiF(400) and LiF(600) analyzing crystals are shown in Fig. 6. By comparison with Fig. 5 one can see that at $q=0$, the resolution effects are of the order of 7–8%.

B. Li Experiments

In this case a series of measurements were made on a 1-in.-diam by 1-in.-long cylindrical single crystal which was rotated around its axis to search for anisotropy and a $\frac{1}{4}$-in.-thick flat poly-

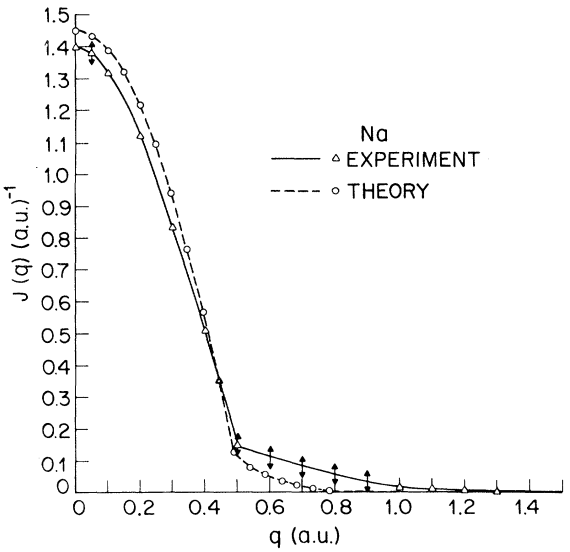

FIG. 5. Compton profile of polycrystalline Na: solid line, experiment (data from Table I); dashed line, theory [identical to curve (a) of Fig. 7].

crystalline sample to obtain an accurate average Compton profile. The experimental results for both samples are shown in Table II. It is immediately obvious from that table that multiple-scattering effects which broaden out the Compton profile were present in the thick Li sample. However, since the thick-crystal data were intended as a search for anisotropy the 10% error produced by multiple scattering will only make our anisotropy measurements 10% too small. Since the maximum anisotropy at $J(0)$ was 4% and our accuracy of measurements was only about 1%, the multiple-scattering effects are small compared to our uncertainty of measurement. It is also worthwhile to note that the thin polycrystalline result obtained here gives a larger value for $J(0)$ and a smaller tail above p_F than all the previous Li results.

TABLE I. Experimental Compton profile for Na.

q	$J(q)$
0	1.398
0.1	1.317
0.2	1.222
0.3	0.835
0.4	0.510
0.5	0.153
0.6	0.115
0.7	0.088
0.8	0.062
0.9	0.040
1.0	0.020
1.1	0.018
1.2	0.014
1.3	0.005
1.4	0.001

TABLE II. Experimental Compton profiles for Li.

	$J(q)$			
q	Thick Li ⟨100⟩	Thick Li ⟨110⟩	Thick Li ⟨111⟩	Thin polycryst.
0	1.037	1.027	1.058	1.125
0.1	1.018	1.014	1.030	1.075
0.2	0.919	0.931	0.941	0.989
0.3	0.773	0.814	0.789	0.819
0.4	0.599	0.624	0.594	0.602
0.5	0.402	0.418	0.402	0.351
0.6	0.187	0.225	0.213	0.154
0.7	0.134	0.159	0.155	0.114
0.8	0.100	0.106	0.114	0.093
0.9	0.072	0.074	0.084	0.079
1.0	0.057	0.048	0.069	0.061
1.1	0.052	0.032	0.050	0.041
1.2	0.048	0.015	0.024	0.033
1.3	0.039	0.012	0.012	0.020
1.4	0.032	0.008	0.003	0.012
1.5	0.021	0.005	0.001	...
1.6	0.016	0.003	...	...
1.7	0.010	...	...	...
1.8	0.004	...	...	...

V. COMPARISON OF THEORY AND EXPERIMENT

A. Sodium

The experimental Compton profile (along with estimated experimental error bars) for the con-

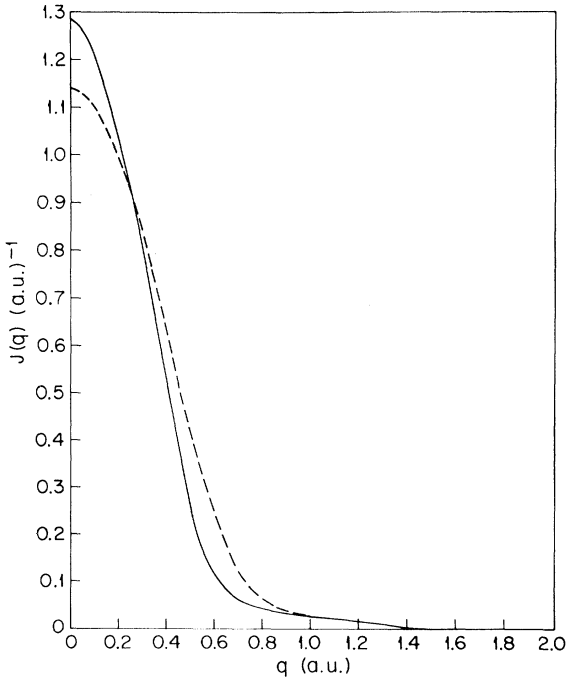

FIG. 6. Experimental Ag results for polycrystalline Na before resolution corrections using LiF(400) (dashed line) and LiF(600) (solid line) analyzing crystal.

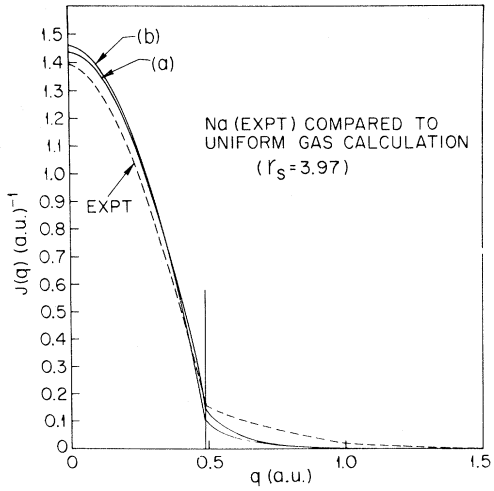

FIG. 7. Experimental Compton profile (identical to that in Fig. 5) of Na (dashed line) compared to various theoretical calculations: curve (a), RPA calculations of Daniel and Vosko (Ref. 10) and Lam (Ref. 14); curve (b), correlation plus exchange calculations of Lam (Ref. 14) and RPA calculation of Lundqvist (Ref. 12). The two different calculations are indistinguishable in the graph. For both curves (a) and (b), $r_s = 3.97$.

duction electrons of sodium is plotted in Fig. 5. Theoretical calculations taking $W_{\langle 110\rangle} = 0.02$ Ry (consistent with a band gap $\Delta_{\langle 110\rangle} \cong 0.04$ Ry) in Eq. (28) and keeping only the 12 smallest reciprocal-lattice vectors gave a maximum anisotropy in $J(0)$ of 0.15%. The same $W_{\langle 110\rangle}$ parameter, more or less independent of the choice of the homogeneous momentum density $N_{\vec{p}}^0$, gives a correction $\Delta N_{\vec{p}}$ of about 0.2% for $J(0)$. These corrections are much too small to be significant. The two distinct theoretical curves shown in Fig. 7 are obtained from published work on the momentum densities of the homogeneous electron gas.[10,12,14] The curve labeled (a) is obtained by numerical interpolation from the results of Daniel and Vosko[10] and Lam.[14] Their results were interpolated to a r_s value of 3.97 and the appropriate integral [see Eq. (5)] performed to give the Compton profile.

In both calculations the authors evaluate the self-energy $\Sigma(\vec{p},\omega)$ of an electron in the RPA and then evaluate the Green's function G to lowest order in Σ^{RPA}, i.e.,

$$G = G_0 + G_0 \Sigma^{\mathrm{RPA}} G_0 \ . \tag{31}$$

The curve labeled (b) is really a composite of two curves which, for this value of r_s, are coincidentally numerically indistinguishable.

(i) The calculation of Lam[14] extends his earlier RPA calculation by including lowest-order exchange in the self-energy but maintaining the approximation given by Eq. (31). Exchange acts to keep parallel-spin electrons apart, thus reduce the probability of short-range encounters. For this reason we expect exchange to reduce the high-momentum tail.

(ii) The calculation of Lundqvist[12] is strictly RPA. It differs from the earlier work shown in Fig. 7(a) in that it includes the complete geometric sum in the calculation of G, i.e.,

$$G = \frac{1}{\omega - p^2/2m - \Sigma^{\mathrm{RPA}}(\vec{p},\omega)} \ . \tag{32}$$

It is not immediately obvious why this calculation so closely corresponds to the exchange-corrected results of Lam.

All three theoretical curves (two of them coincident) are in significant disagreement with the dashed experimental curve. The theoretical estimates differ by about 3% at $q = 0$ and there is about twice as much area above p_F in the experiment as in the simplest version of the theory.

It is not possible to fix up the disagreement between theory and experiment by simply increasing the value of r_s. The effect of doing this for the RPA results of Lam is shown in Fig. 8. Increasing r_s, does, as expected, slightly increase the size of the tail. The amount of the increase is still too small, and, apparently, the shape is still incorrect. The experimental spectrum seems to be noticeably flatter.

We will return to a discussion of these discrepancies in Sec. VI.

Assuming that the experimental profile reflects the properties of the homogeneous gas it is possible to extract the renormalization constant Z_{p_F}. The break in slope at p_F is a direct measure of this quantity (see Sec. III). In Fig. 9 we show the ex-

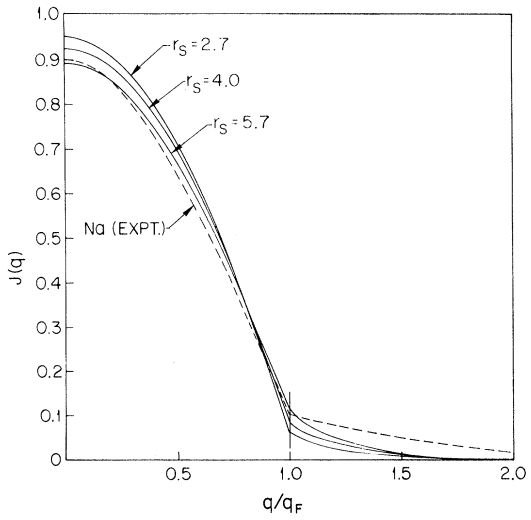

FIG. 8. Rescaled experimental Compton profile of Na (dashed line) compared to RPA calculations of Lam (Ref. 14) assuming various values of r_s.

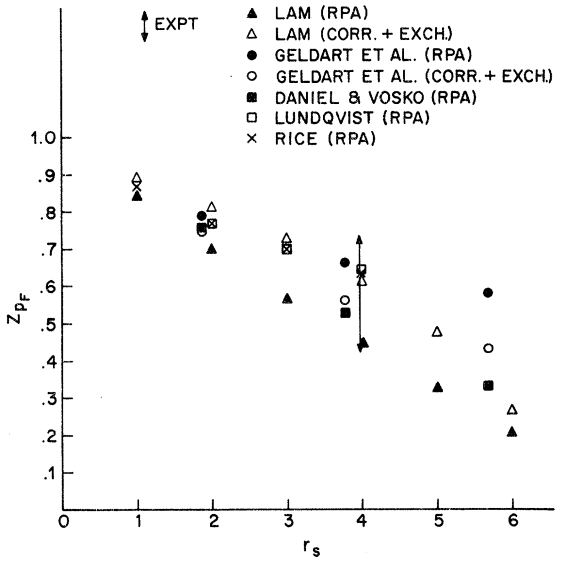

FIG. 9. Renormalization constant Z_{p_F} vs r_s. The theoretical points are ▲, RPA (Lam, Ref. 14); △, correlation plus exchange (Lam, Ref. 14); ●, RPA (Geldart *et al.* Ref. 11); ○, correlation plus exchange (Geldart *et al.*, Ref. 11); ■, RPA (Daniel and Vosko, Ref. 10); □, RPA (Lundqvist, Ref. 12); ×, RPA (Rice, Ref. 25).

perimental point at $r_s = 3.97$ along with the results of several calculations, for varying r_s, of this quantity.

B. Lithium

For Li, $r_s = 3.22$ and we obtain the homogeneous part of the momentum distribution in the same way as we obtained it for Na, i.e., by interpolating the various published RPA results. The homogeneous portion of $N_{\vec{p}}$ is only about 0.2 of the measured spectrums in the tail region.

Unlike the case of Na the inhomogeneous term is not only significant in the case of Li but dominates the tail of the Compton profile. For this reason some care must be exercised in the choice of the lattice potential. Equation (30) tells us that $W_{\vec{G}}$ is determined by the band gap $\Delta_{\vec{G}}$ and the quantities Z_{p_F} and $\tilde{\Lambda}_4^\infty$. While the value of $\Delta_{\vec{G}}$ is relatively well known from experiment, numerical calculations for Z_{p_F} and $\tilde{\Lambda}_4^\infty$ range from 1.06 [24] to 1.8 [25] and Z_{p_F} runs from 0.53 [14] to 0.69. [12,25] Using a $\Delta_{\langle 110\rangle} = 0.22$ Ry [26] the various combinations of the above figures give the range of $W_{\langle 110\rangle}$ from 0.1 to 0.2 Ry. This value of $W_{\langle 110\rangle}$ is for $|G| = 1.143$ $(2p_F)$, the shortest one in a bcc crystal. In addition to the 12 shortest $\langle 110\rangle$ $\vec{G}$'s we want to keep as well the six next-shortest ones ($\langle 100\rangle$) in Eq. (28). Each of these six has lengths 1.616 $(2p_F)$ and, therefore, should have a different value ($W_{\langle 100\rangle}$) from $W_{\langle 110\rangle}$ given above. Instead of directly calculating $W_{\langle 100\rangle}$ for this new set of six, we assume that it can be obtained from the relation

$$W_{\langle 100\rangle} = W_{\langle 110\rangle} |\varphi_2/\varphi_1|^2 , \tag{33}$$

where φ_1, φ_2 are the pseudopotentials of Li at the shortest and next-shortest G's, respectively. From the curve of Animalu and Heine, [27] we find that $|\varphi_2/\varphi_1| = 0.64$. The error introduced by using Eq. (33) is minimal since the contribution to the Compton profile from the second set is small, usually an order of magnitude less than that of the first set. It does, however, have the effect of smoothing out the bumps found in the profiles. Calculated results for the Compton profile of Li utilizing Lam's RPA results for the homogeneous part [14] and $W_{\langle 100\rangle} = 0.15$ Ry are plotted in Fig. 10. All curves have the same area.

As shown in Fig. 10 the following features immediately present themselves.

(i) The anisotropy is appreciable. At the origin, the difference between the profiles amounts to ~4% of $J(0)$. $J(0)$ for $\hat{k} \parallel \langle 111\rangle$ is greater than that for $\hat{k} \parallel \langle 100\rangle$ which, in turn, is greater than that for $\hat{k} \parallel \langle 110\rangle$. This can be easily understood by noting that the area under each profile is conserved and that the number of secondary m surfaces (defined in Sec. II) in the space $q > p_F$ is in reverse order for the different directions of $\vec{k}$. In fact, out of the important 12 $\vec{G}$'s nearest to the origin, there are three of them in the space $q > p_F$ beyond the plane $q = p_F$ cutting the $\langle 111\rangle$ axis, while the number increases to four and five, respectively, for $\hat{k}$ parallel to $\langle 100\rangle$ and $\langle 110\rangle$. We thus see that the relative magnitude of the profiles at the

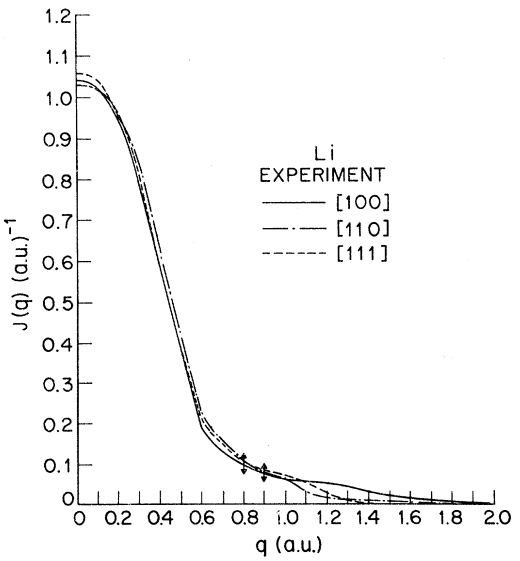

FIG. 10. Theoretical Compton profiles of Li for various directions of momentum transfer $\hat{k}$: solid line, $\hat{k} \parallel \langle 100\rangle$; dot-dashed line, $\hat{k} \parallel \langle 110\rangle$; dashed line, $\hat{k} \parallel \langle 111\rangle$. $W_{\langle 110\rangle} = 0.15$ Ry in Eq. (28).

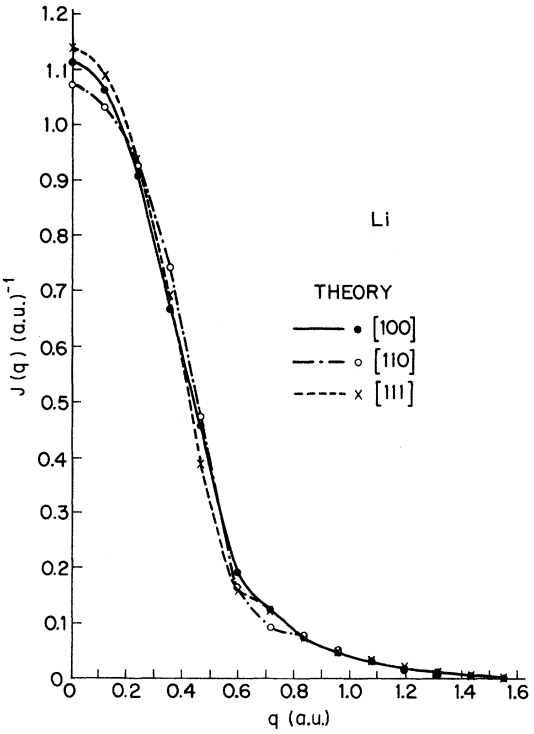

FIG. 11. Experimental Compton profiles of single-crystal Li for various directions of momentum transfer $\hat{k}$: solid line, $\hat{k} \parallel \langle 100 \rangle$; dot-dashed line, $\hat{k} \parallel \langle 110 \rangle$; dashed line, $\hat{k} \parallel \langle 111 \rangle$. Sample is 1 in. thick; multiple-scattering processes involved.

origin mainly reflects the geometry of the reciprocal lattice. Their absolute magnitudes depend on the strength of the electron-ion interaction.

(ii) The profiles vanish at about $2.6p_F$ because of the rapid falloff of $N_{\vec{p}}^0$.

(iii) The main cusp point for each of the profiles is located at the same point, $p = p_F = 0.596$ a.u.

(iv) The height of the main cusp point varies for different directions of k.

(v) Little bumps appear in the tail for $\hat{k} \parallel \langle 111 \rangle$ and $\langle 110 \rangle$.

Secondary cusp points do exist in our calculations as predicted in Sec. II but are not marked in Fig. 10 because they are too weak to show up.

A comparison of the single-crystal experimental data (shown in Fig. 11) with the theoretical Compton profiles (shown in Fig. 10) indicates that the first four features are confirmed and that the experiment is not good enough to either confirm or negate the last prediction.

In Fig. 12 we present a quantitative comparison of the theoretical profiles with the polycrystalline data. The theoretical points are calculated with several different values of $W_{\langle 110 \rangle}$, viz., 0.10, 0.15, and 0.20 Ry, respectively. The homogeneous part is the same as that used in Fig. 10. It is clear that the curve with $W_{\langle 110 \rangle} = 0.15$ Ry is very close to the experiment. This value of $W_{\langle 110 \rangle}$ corresponds to $|Z_{p_F} \tilde{\Lambda}_4^\infty| = 0.73$ (assuming $\Delta_{\langle 110 \rangle} = 0.22$ Ry) which may then be broken down to agree with the theoretical value of $Z_{p_F} = 0.69$[12,25] and $\tilde{\Lambda}_4^\infty = 1.06$.[24] However, it is also true that the uncertainty in the choice of W allows one to fit a wide range of data.

For an anisotropic electron gas, the break in slope does *not* give the renormalization constant since the higher m spheres contribute to the break. Within the approximation given by Eq. (15), and for parameters characteristic of Li we find that the contribution due to $\Delta N_{\vec{p}}$ is negligible. The experimental situation is not absolutely clear since it is by no means trivial to obtain the slopes from the experimental curves because of significant finite resolution effects. These resolution effects tend to wash out the details near the break making the exact size of the break, particularly in Li, uncertain. For this reason the experimental Z_{p_F} for Li has not been included in Fig. 9. However, as shown in Fig. 12, the experimental result is certainly consistent with the predictions of the theory.

VI. DISCUSSION

While there are significant areas of disagreement between the theory and experiment presented here the areas of agreement seem to indicate where this discrepancy might come from.

The results presented in Sec. V clearly show that the relative amount of area (for $p > p_F$) in the Compton profiles is larger in Li than in Na. This is contrary to the predictions of calculations where both metals are viewed as homogeneous interacting electron liquids. The large tail in Li must be understood as a manifestation of the dominating role of the relatively large electron-ion interaction, i.e., size of $W_{\vec{G}}$.

Quantitatively the weak pseudopotential approach does, with very little adjustment, give a relatively good fit to the complete anisotropic Compton profiles. We can easily understand the good quantitative agreement with the anisotropy data in spite of the fact that this same kind of approach does not work in predicting the details of the band structure. These particular features of the Compton profile as discussed depend primarily on the geometry of the secondary m surfaces (i.e., the lattice structure) and not on the exact value of the external potential.

The fit to the shape and size of the polycrystalline profile of Li with reasonable values of $W_{\vec{G}}$ is particularly remarkable. On the other hand, the deficiency in the tail of Na may simply come from errors in the calculations for the homogeneous electron gas. In fact, if the homogeneous part is

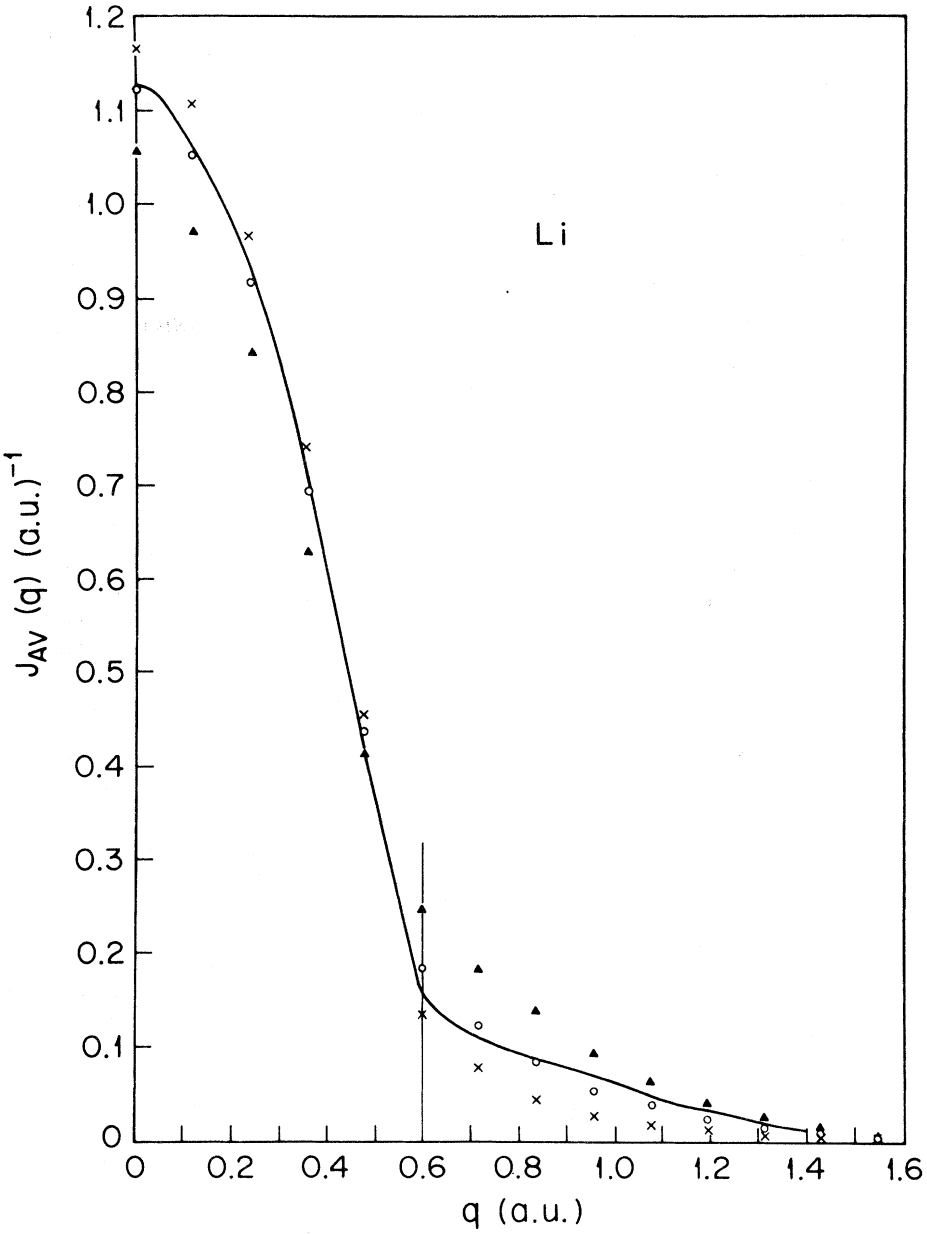

FIG. 12. Experimental Compton profile of polycrystalline Li (solid line) compared with theoretical predictions from Eqs. (5), (15), and (28). The different set of theoretical points corresponds to different values of $W_{\langle 110\rangle}$ in Eq. (28). For ×, $W_{\langle 110\rangle}$ = 0.10 Ry; ○, $W_{\langle 110\rangle}$ = 0.15 Ry; ▲, $W_{\langle 110\rangle}$ = 0.20 Ry.

arbitrarily raised to fit the Na tail, we will still get a good fit to Li data with a slightly different value of $W_{\vec{G}}$, since the tail in Li is dominated by the secondary m surfaces anyway. Of course, it is also possible that the conventional perturbation calculation of the homogeneous system presented here is just not valid, i.e., that

$$H_0 \equiv \sum_i p_i^2/2m \tag{34}$$

is not the correct starting point in a perturbation calculation. If this is indeed the case then we will be forced to deal with a system of interacting band electrons where core orthogonalization[28] and the modified energy momentum relation of the band electrons, two effects which have been ignored in this calculation, will come into play. More investigations along this line are planned.

Further experiments of higher accuracy will be of interest in checking the fine structures of the Compton profiles predicted here. We also note that the Na experiment is, in many ways, the most difficult Compton experiment to perform. The first difficulty arises because it is such a sharp profile which, as we have shown, requires that considerable resolution corrections be made. Second, because we are just interested in the proper-

ty of one of the 11 Na electrons, one has a large background to subtract. We feel we have coped successfully with those difficulties but another independent quantitative measurement of Na would still be welcomed.

ACKNOWLEDGMENT

Acknowledgment of the considerable technical and computational assistance of W. C. Marra is gratefully given.

*Resident visitor from Department of Physics, Columbia University, New York, N. Y.

[1]J. W. M. DuMond, Phys. Rev. 33, 643 (1929).

[2]P. M. Platzman and N. Tzoar, Phys. Rev. 139, A410 (1965).

[3]W. C. Phillips and R. J. Weiss, Phys. Rev. 171, 790 (1968).

[4]M. Cooper, J. A. Leake, and R. J. Weiss, Phil. Mag. 12, 797 (1965).

[5]P. Eisenberger and P. M. Platzman, Phys. Rev. A 2, 415 (1970).

[6]P. Eisenberger, Phys. Rev. A 2, 1678 (1970); 5, 628 (1972).

[7]P. Eisenberger, W. H. Henneker, and P. E. Cade, J. Chem. Phys. 56, 1207 (1972).

[8]B. I. Lundqvist and C. Lydén, Phys. Rev. B 4, 3360 (1971).

[9]J. Callaway, Phys. Rev. 127, 1913 (1962); F. Ham, *ibid.* 128, 82 (1962).

[10]E. Daniel and S. H. Vosko, Phys. Rev. 120, 2041 (1960).

[11]D. J. W. Geldart, A. Houghton, and S. H. Vosko, Can. J. Phys. 42, 1938 (1964).

[12]B. I. Lundqvist, Physik Kondensierten Materie 7, 117 (1968).

[13]A. W. Overhauser, Phys. Rev. B 3, 1888 (1971).

[14]J. Lam, Phys. Rev. B 3, 3243 (1971).

[15]L. Lam and P. M. Platzman (unpublished).

[16]J. M. Luttinger, Phys. Rev. 119, 1153 (1960).

[17]L. Lam and P. M. Platzman, Bull. Am. Phys. Soc. 16, 1428 (1971); 17, 270 (1972).

[18]R. P. Feynman, Phys. Rev. 56, 340 (1939).

[19]V. Heine, P. Nozières, and J. W. Wilkins, Phil. Mag. 13, 741 (1966).

[20]P. Nozières, *Theory of Interacting Fermi System* (Benjamin, New York, 1964).

[21]M. Cooper, B. G. Williams, R. E. Borland, and R. A. Cooper, Phil. Mag. 22, 441 (1970).

[22]R. Currat, P. D. DeCicco, and R. J. Weiss, Phys. Rev. B 4, 4256 (1971).

[23]W. Phillips and R. J. Weiss, Phys. Rev. B 5, 755 (1972).

[24]D. C. Langreth, Phys. Rev. 181, 753 (1969).

[25]T. M. Rice, Ann. Phys. (N.Y.) 31, 100 (1965).

[26]J. J. Donaghy and A. T. Stewart, Phys. Rev. 164, 391 (1967).

[27]A. O. E. Animalu and V. Heine, Phil. Mag. 12, 1249 (1965).

[28]Preliminary estimates of the core-orthogonalization effects by K. Pandy and B. I. Lundqvist (private communications) seem to indicate that as much as 6% of the area in the Compton profile for the conduction electrons below p_F may be transferred to momenta above p_F.

PHYSICAL REVIEW B VOLUME 6, NUMBER 10 15 NOVEMBER 1972

Evidence of Two Simultaneous Mechanisms for Diffusion of Cu in Pb Single Crystals*

A. Ascoli and G. Poletti
Centro Informazioni Studi Esperienze, Segrate Milano, Italy
(Received 24 April 1972)

The radioactive-tracer method and sectioning technique were used to measure the diffusion coefficient of Cu in Pb single crystals under hydrostatic pressures between 1.75 and 9.00 kbar, at temperatures between (206 ± 1) and (326 ± 1) °C. The diffusivity at 1.75 kbar is described by $D_{1.75} = 0.95 \times 10^{-2} e^{-8800/RT}$ cm^2/sec^{-1}, which is in good agreement with previoulsy published results; the diffusivity between 3 and 9 kbar is described by $D_{3 \text{ to } 9} = 6.18 \times 10^{-2} e^{-10\,900/RT}$ cm^2/sec^{-1}. Average activation volumes between $P = 0$ and 1.75 kbar are in the range of $0.7V$ (V is the atomic volume of Pb); above $P = 3.38$ kbar, they are nearly zero.

I. INTRODUCTION

Diffusion results were interpreted for many years on the basis of single mechanisms. Recent evidence, particularly from pressure-diffusion[1-5] and related[6] experiments pointed to the possible coexistence of more than one mechanism in certain single solvent–solute systems. The diffusion of noble metals in lead looks interesting seen in this context. Intermetallic diffusion in all other fcc solvents is attributed to a vacancy mechanism, but the low values of the activation energy Q for the diffusion of noble impurities in lead were interpreted[7-11] on the basis of interstitial mechanisms.

Van der Maesen and Brenkman[12] first proposed that copper dissolves both interstitially and substitutionally in germanium. Ascoli *et al.*, on the basis of pressure-diffusion results[3] and almost